International Journal of Hydrogen Energy 287 (2026) 158200

Contents lists available at ScienceDirect

International Journal of Hydrogen Energy

journal homepage: www.elsevier.com/locate/he

Investigation of mechanism for hydrogen-assisted crack propagation in austenitic stainless steels using acoustic emission method

Ryutaro Matsumoto [a,b], Kaita Ito [c], Luthfan Adhy Lesmana [b], Takashi Iijima [d], Hirotoshi Enoki [d], Tetsuya Uchimoto [b,e,*]

[a] Department of Mechanical Engineering, Tohoku University, 6-6, Aramaki Aza Aoba, Aoba-ku, Sendai, Miyagi, 980-8579, Japan
[b] Institute of Fluid Science, Tohoku University, 2-1-1 Katahira, Aoba-ku, Sendai, Miyagi, 980-8577, Japan
[c] Center for Basic Research on Materials, National Institute for Materials Science (NIMS), 1-1, Namiki, Tsukuba, Ibaraki, 305-0044, Japan
[d] National Institute of Advanced Industrial Science and Technology (AIST), 16-1, Onogawa, Tsukuba, Ibaraki, 305-8569, Japan
[e] ELyTMaX IRL3757, CNRS, Univ. Lyon, INSA Lyon, Centrale Lyon, Université Claude Bernard Lyon 1, Tohoku University, 2-1-1 Katahira, Aoba-ku, Sendai, Miyagi, 980-8577, Japan

ARTICLE INFO

Keywords:
Hydrogen embrittlement
Acoustic emission
Austenitic stainless steels
Fatigue test
DBSCAN

ABSTRACT

Hydrogen embrittlement is a critical issue for structural materials used in high-pressure hydrogen systems, where cyclic loading can accelerate fatigue crack propagation. This study investigates the effect of hydrogen on fatigue crack propagation in AISI 304 austenitic stainless steel using acoustic emission (AE) method. Specimens were prepared under uncharged and hydrogen-charged (exposed to high-pressure hydrogen gas) conditions. Fatigue crack propagation tests were conducted under constant stress intensity factor ranges (ΔK), during which AE signals were continuously recorded, and the DBSCAN algorithm was applied to classify and extract distinct AE event groups. Comparative analysis of the stress phase at AE initiation suggested that hydrogen charging can be associated with a lower initiation phase and a reduced dependency on ΔK. This behavior may be associated with changes in crack-opening-related AE activity and less apparent variation across the three tested ΔK conditions. Furthermore, the frequency characteristics of the AE clusters showed smaller apparent variations among the three ΔK conditions after hydrogen charging. These differences may reflect changes in crack-tip deformation and crack-propagation behavior, although the underlying AE source mechanisms could not be uniquely identified. Meanwhile, verification of the AE RMS voltage indicated that the strain-induced martensitic transformation itself was difficult to detect directly via the AE method under the present experimental conditions.

1. Introduction

Hydrogen has attracted considerable attention as a next-generation energy carrier across various industrial sectors, creating an urgent need to expand the deployment of hydrogen stations to establish a reliable supply infrastructure [1]. However, hydrogen embrittlement (HE) remains a critical challenge in the utilization and storage of hydrogen. HE is a degradation phenomenon wherein hydrogen penetrates and dissolves into the material from the surrounding environment, leading to a significant reduction in the strength and ductility [2]. In high-pressure hydrogen environments, such as those encountered in hydrogen stations, austenitic stainless steels are primary structural materials owing to their relatively high resistance to HE [3]. The structural materials of hydrogen stations are subjected to cyclic stress due to system operations such as hydrogen refueling of the vehicles. Under these conditions, the combined effects of cyclic stress and hydrogen exposure can accelerate fatigue crack initiation and propagation, leading to hydrogen-assisted fatigue failure.

Previous experimental findings have been reported regarding the effects of hydrogen on the fatigue properties in austenitic stainless steels. First, the presence of hydrogen influences the fracture surface morphology during fatigue crack growth. While the uncharged specimens exhibit a ductile fracture surface characterized by dimples, the hydrogen-charged specimens display quasi-cleavage fracture surface [4–7]. Second, hydrogen affects the plastic deformation behavior around the crack tip. The plastic zone in the hydrogen-charged specimens is confined to a smaller region near the crack tip compared to that in the uncharged specimens [8–10]. Third, the effect of hydrogen on

* Corresponding author. Institute of Fluid Science, Tohoku University, 2-1-1 Katahira, Aoba-ku, Sendai, Miyagi, 980-8577, Japan.
E-mail address: uchimoto@tohoku.ac.jp (T. Uchimoto).

https://doi.org/10.1016/j.ijhydene.2026.158200
Received 31 July 2026; Received in revised form 5 October 2026; Accepted 16 October 2026
Available online 26 October 2026
0360-3199/© 2026 The Author(s). Published by Elsevier Ltd on behalf of Hydrogen Energy Publications LLC. This is an open access article under the CC BY license (http://creativecommons.org/licenses/by/4.0/).

austenite stability has also been widely discussed; it has been reported that strain-induced martensitic transformation at the crack tip is markedly suppressed in the hydrogen-charged material compared to the uncharged material [2,11,12].

Based on these experimental findings, several theories, such as hydrogen-enhanced decohesion (HEDE) [13,14] and hydrogen-enhanced localized plasticity (HELP) [10,15], have been proposed to explain the mechanisms of HE. However, the influence of hydrogen on the mechanical behavior of materials is highly complex, and no unified consensus has been established [16].

Various methodologies have been utilized to evaluate HE. From a microscopic perspective, characterizations of fracture morphologies and microstructural evolution have been conducted; Murakami et al. [17] reported the acceleration mechanism of localized plastic deformation at the crack tip, while Koyama et al. [18] characterized the initiation and propagation pathways of hydrogen-induced cracking using electron microscopy techniques. Regarding the state of hydrogen and lattice defects, Choo et al. [19] quantitatively evaluated the hydrogen trapping characteristics via thermal analysis. Non-destructive testing (NDT) techniques have also been introduced; Takeda et al. [20] successfully quantified the crack-tip martensitic transformation and crack closure behavior by complementarily applying eddy current testing and ultrasonic testing. However, most of these approaches are limited to post-test evaluations, and studies focusing on the real-time, continuous monitoring of hydrogen effects during crack propagation remain limited.

In this study, acoustic emission (AE) method was adopted as a method for *in-situ* evaluation of the effect of hydrogen on fatigue crack propagation. The AE method is a type of NDT which typically uses piezoelectric sensors attached to the surface of an object to detect the elastic (AE) waves generated when solid materials are deformed or fractured. AE method is a highly sensitive monitoring technique for detecting phenomena associated with fatigue, such as the initiation and propagation of microcracks and friction. To date, several studies have monitored hydrogen embrittlement using the AE method. Dunegan et al. [21] applied the AE technique to hydrogen-assisted crack propagation in high-strength steels, demonstrating that the time-to-failure could be predicted based on the relationship between the stress intensity factor K and the AE count rate. Additionally, Shiraiwa et al. [22] identified the moment of hydrogen-induced cracking in martensitic steel welds in real time during slow strain rate tensile (SSRT) tests. Furthermore, Jiang et al. [23] achieved the automatic identification of hydrogen-induced cracks under noisy environments during SSRT tests of high-pressure hydrogen-charged AISI 304 austenitic stainless steel by combining machine learning with AE waveform. However, previous investigations have primarily focused on the "monitoring of phenomena or the establishment of predictive methodologies using AE method," such as detecting hydrogen-induced cracking under static loads or predicting fatigue life. Consequently, the application of multi-parameter analysis of AE signals to evaluate and elucidate how hydrogen alters the fatigue characteristics themselves remain insufficient.

Based on this background, this study conducts real-time AE measurements during fatigue crack propagation tests on AISI 304 austenitic stainless steel hydrogen-charged via high-pressure hydrogen gas exposure. The objective is to evaluate the effects of hydrogen on the fatigue crack propagation process by multi-parameter analysis of AE. To effectively process the intricate elastic wave signals, a density-based spatial clustering of applications with noise (DBSCAN) algorithm is implemented using key AE parameters to classify the detected AE events.

2. Methods

2.1. Specimen and fatigue testing

AISI 304 austenitic stainless steel was used in this study. Table 1 shows the chemical composition of the test metal used to prepare the specimens. The test metals were solution-treated at 1120 °C for 10 min.

Table 1
Chemical composition of AISI 304 austenitic stainless steel (wt.%).

C	Si	Mn	P	S	Ni	Cr	Co
0.04	0.53	0.90	0.035	0.001	8.05	18.11	0.18

Therefore, no special consideration was given to the rolling direction for any of the test specimens.

The dimensions of the specimens were determined in accordance with ASTM E647 [24]. Fig. 1 illustrates the geometry of the compact tension (CT) specimen used in this study.

Two types of specimens were prepared: hydrogen-charged and uncharged specimens. The hydrogen charging was performed by exposing the specimens to high-pressure hydrogen gas at 270 °C and 100 MPa for 323 h. Two specimens were tested for each combination of hydrogen-charging condition and fatigue-test condition, resulting in a total of 12 specimens. After hydrogen charging, the specimens were transported by refrigerated courier service at approximately 0–10 °C, with a transfer time of approximately 24 h. The specimens were subsequently stored in a household freezer until fatigue testing. Because hydrogen diffusion in austenitic stainless steel is relatively slow at room temperature [17], refrigerated transport and freezer storage were expected to reduce hydrogen desorption. Nevertheless, the hydrogen concentration was not measured after transport or storage; therefore, the extent of hydrogen loss could not be quantified in the present study.

Fatigue tests were conducted using a horizontal fatigue testing machine (Lab-5, SHIMADZU), under a constant stress intensity factor range ΔK. Fatigue testing conditions are summarized in Table 2. The primary test conditions comprised three combinations of ΔK [MPa$\sqrt{\text{m}}$] and the stress ratio R: (ΔK, R) = (30, 0.1), (20, 0.1), and (15, 0.1). These tests were performed using a sinusoidal waveform at a frequency of 1.0 Hz until the crack length a reached 22 mm (a/W = 0.433). Because the objective of the present study was to characterize AE behavior during stable fatigue crack propagation, sufficient AE data had been obtained over the crack-growth interval by this point. The tests were therefore terminated at a = 22 mm rather than continued to larger a/W. All tests were carried out at room temperature in an atmospheric environment. Prior to the main testing, a 3.0-mm pre-crack was introduced at a frequency of 10 Hz under the same ΔK and R conditions as the subsequent fatigue tests.

2.2. AE measurement

AE was monitored during the fatigue tests. Two wideband AE sensors (type WSα, Physical Acoustic Corporation) with a frequency range of 100–1000 kHz were mounted in holders attached to the side surface of the CT specimen. Glycerin paste (BS-400, Nippon Sanso Gas & Welding Corporation) was used as the couplant between the sensors and the

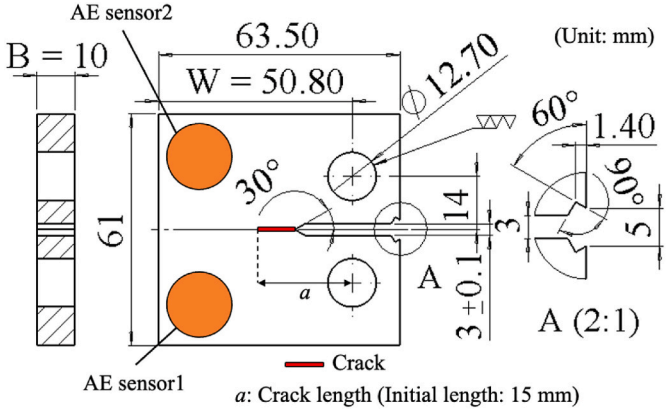


Fig. 1. Dimension of the CT specimen.

Table 2
Fatigue testing conditions.

ΔK (MPa$\sqrt{\text{m}}$)	R
30	0.1
20	0.1
15	0.1

specimen surface. The gain of the preamplifier (type 2/4/6, Physical Acoustic Corporation) was set to 40 dB. For AE measurement, the Continuous Wave Memory (CWM) system developed by Ito, one of the authors of this paper [25–27], was used. The sampling frequency was set to 5 MHz, the voltage range to ±5 V. The AE hit detection thresholds were set to 65, 60, and 50 dB for $\Delta K = 30$, 20, 15 MPa$\sqrt{\text{m}}$, respectively. Note that 0 dB corresponds to 0.1 mV. The threshold is expressed as the voltage value after passing through the amplifier. To avoid mistaking sudden noise for an AE event, a valid AE event was considered only when both sensors exceeded the threshold voltage within a trigger time difference of 100 μs or less. Furthermore, the load signal from the fatigue testing machine was synchronously measured with the AE signals and recorded as data at a sampling frequency of 1 kHz. Fig. 2 shows a schematic diagram of the experimental setup, highlighting the AE measurement system integrated with the fatigue testing machine. The AE hit-detection thresholds were selected according to the residual noise level after noise filtering for each test condition. Because the detection thresholds differed among the ΔK conditions, absolute AE event counts and amplitude distributions were not used for direct quantitative comparison among the three ΔK levels. The subsequent analysis instead focused primarily on the temporal and phase distributions of persistent AE-event groups.

The residual noise level was higher at larger ΔK; therefore, thresholds of 65, 60, and 50 dB were adopted for ΔK = 30, 20, and 15 MPa$\sqrt{\text{m}}$, respectively. Applying a common threshold of 65 dB to all conditions would substantially reduce the number of detectable AE events at ΔK = 15 MPa$\sqrt{\text{m}}$. Therefore, condition-specific thresholds were used to maintain sufficient AE sensitivity while suppressing residual noise. The residual noise level increased at higher ΔK; therefore, thresholds of 65, 60, and 50 dB were used for ΔK = 30, 20, and 15 MPa$\sqrt{\text{m}}$, respectively. A common threshold of 65 dB would substantially reduce the number of detectable AE events at ΔK = 15 MPa$\sqrt{\text{m}}$. Accordingly, condition-specific thresholds were used to maintain sufficient sensitivity while suppressing residual noise. Peak frequency was defined as the frequency corresponding to the maximum intensity in the FFT spectrum.

Crack length was determined from the compliance measured using a clip gauge. The applied load was adjusted according to the measured crack length to maintain the prescribed ΔK. The crack-growth rate, da/dN, was calculated using a local polynomial fit to three consecutive crack-length data points, evaluated at the central point.

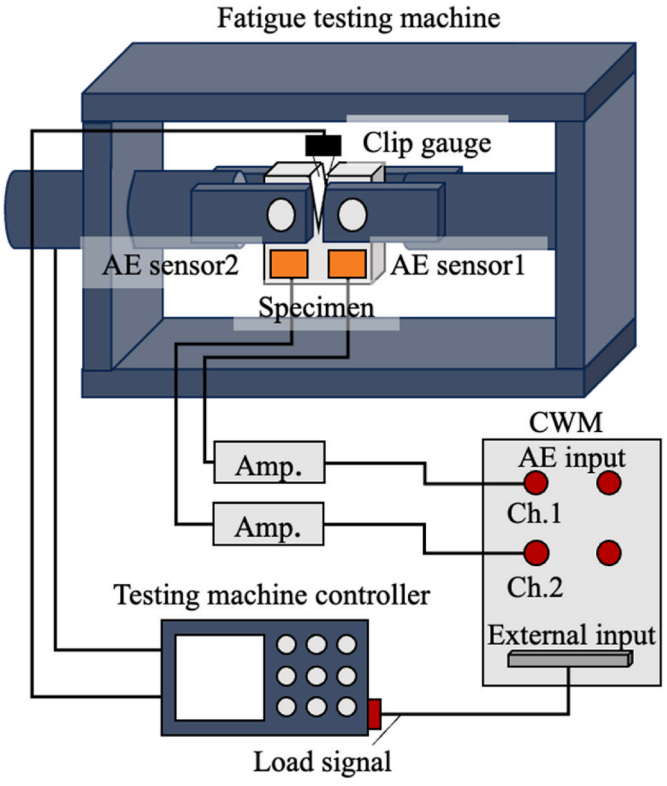


Fig. 2. Schematic image of fatigue tests and acoustic emission recording system.

2.3. Fractographic observation

Following the fatigue tests, the crack surfaces of the specimens were characterized using a scanning electron microscope (SEM; JSM-7100F, JEOL). As illustrated in Fig. 3, sections containing the fatigue crack growth regions were cut from the specimens using an electrical discharge machine (EDM). The fracture surfaces were then observed at acceleration voltage of 15.0 kV.

2.4. AE event categorization

To extract and classify AE events from the measured signals, a clustering technique, Density-Based Spatial Clustering of Applications with Noise (DBSCAN) [28], was employed. DBSCAN is an algorithm that forms clusters based on the local density of data points; it does not require the prior specification of the number of clusters and can identify clusters of arbitrary shapes while effectively distinguishing noise (outliers) from the core data. The detailed conditions for the DBSCAN applied in this study are described later in this paper.

3. Results and discussion

3.1. Fatigue test results

Fig. 4 shows the crack growth rates for each set of fatigue test conditions. The horizontal and vertical axes represent ΔK and the crack growth rate on a logarithmic scale, respectively. The crack growth rates are higher at higher ΔK. Also, when comparing specimens at the same ΔK, the crack growth rate of hydrogen-charged specimens is higher than that of uncharged specimens. The parameters of Paris' law were determined by the least-squares method for the hydrogen-charged and uncharged specimens. The resulting relationships are expressed as follows:

$$\text{Hydrogen charged specimens } \frac{da}{dN} = 1.41 \times 10^{-6}(\Delta K)^{1.95} \quad (1)$$

$$\text{Uncharged specimens } \frac{da}{dN} = 6.15 \times 10^{-9}(\Delta K)^{3.04} \quad (2)$$

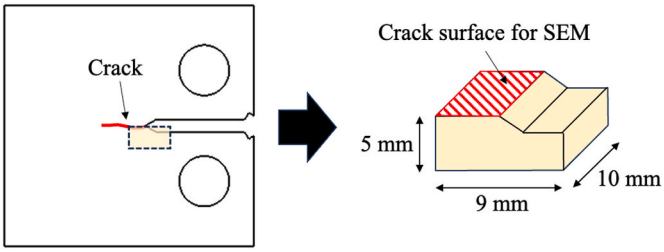


Fig. 3. Schematic illustration of observation area for SEM.

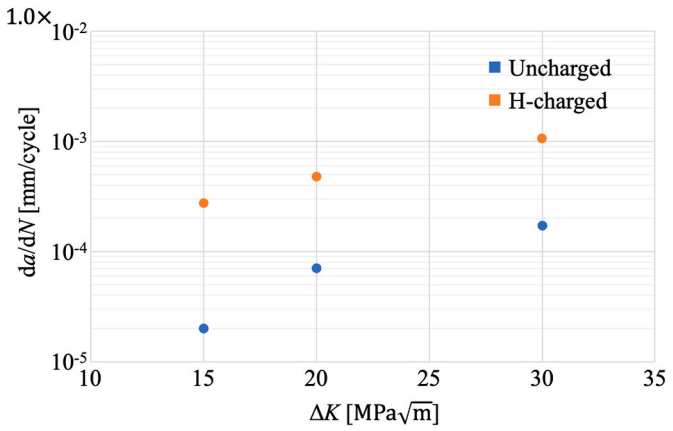


Fig. 4. da/dN vs. ΔK plot.

3.2. Fractographic observation

Fig. 5 shows the SEM images of the uncharged and hydrogen-charged specimens with ΔK of 30 and 15 MPa$\sqrt{\text{m}}$. Observation was conducted from the direction tilted approximately 45° counterclockwise to facilitate dimple observation. Regardless of ΔK, the fracture surfaces of the uncharged specimens were predominantly characterized by dimples. In contrast, the hydrogen-charged specimens exhibited quasi-cleavage fracture surfaces featuring a mixture of dimples and flat regions. Martin et al. [7] reported that hydrogen charging causes a morphological transition of the fracture surface from ductile dimple fracture to quasi-cleavage fracture, which is consistent with our observations. No clear striations were observed in any of the specimens.

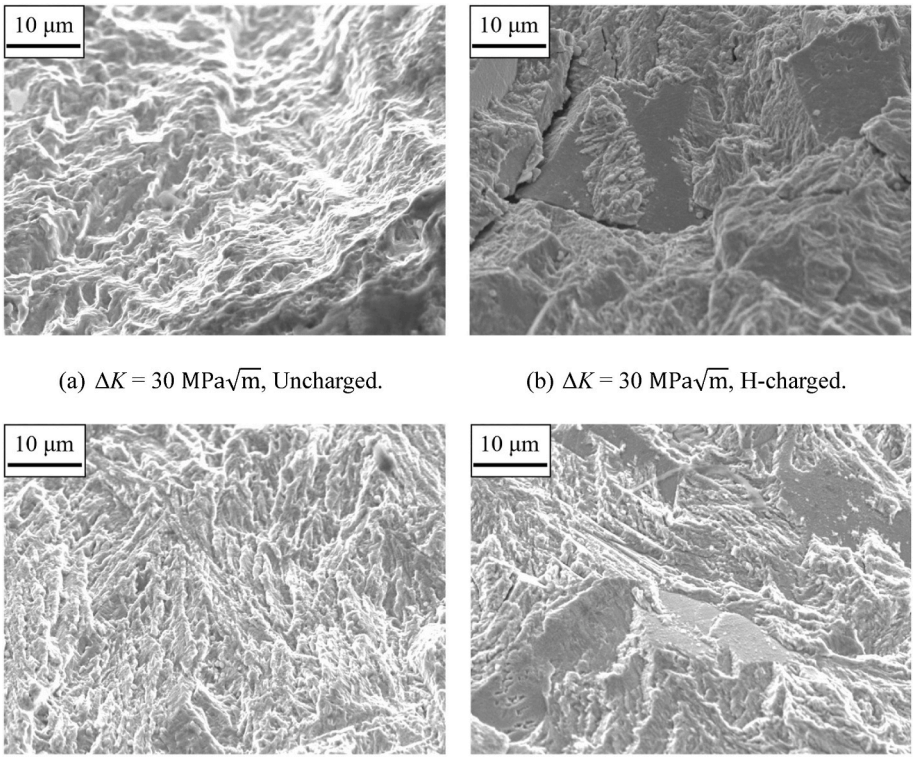
3.3. AE measurements

During the loading stage of the fatigue cycle ($0 \leqq$ phase < 0.5), AE event groups exhibiting continuous phase variation over time were observed, regardless of the testing conditions or the presence of hydrogen charging. This indicates that AE events occur repeatedly at specific phase within the fatigue cycle. Elber [29] reported that due to residual stresses within the plastically deformed zone (plastic wake) left behind the advancing crack tip, the crack faces remain closed and do not contribute to propagation until a certain stress level is reached during the loading stage, thereby proposing the effective stress intensity factor range, ΔK_{eff}. Furthermore, Nonaka et al. [30] demonstrated, through direct SEM observations of AISI 304 austenitic stainless steel, that AE signals are generated not at the maximum load point of the fatigue cycle, but rather at the stage where the crack opens and subsequent propagation initiates. In the present study, the curved AE event groups were also concentrated mainly in the phase range of 0.1 to 0.4, rather than at the maximum stress point (phase = 0.5). Therefore, these AE events are considered to capture the elastic energy released during crack opening or propagation.

To further evaluate these characteristic AE event groups, DBSCAN was applied. The four AE parameters selected for DBSCAN were the trigger time, stress phase, maximum amplitude, and median frequency, which exhibit low correlation. The median frequency is defined as the frequency at which the cumulative intensity reaches 50% of the total intensity in the power spectrum of the AE waveform. Because the scale differences among features significantly affect the clustering performance in DBSCAN, each parameter x was normalized as follows.

$$x' = \frac{x - x_{min}}{x_{max} - x_{min}} \tag{3}$$

where x_{min} and x_{max} denote the minimum and maximum values of the respective feature. Through this normalization, each parameter is scaled



(a) ΔK = 30 MPa$\sqrt{\text{m}}$, Uncharged. (b) ΔK = 30 MPa$\sqrt{\text{m}}$, H-charged.

(c) ΔK = 15 MPa$\sqrt{\text{m}}$, Uncharged. (d) ΔK = 15 MPa$\sqrt{\text{m}}$, H-charged.

Fig. 5. Fracture surface observed by SEM.

within the range of 0 to 1. The four AE parameters used for DBSCAN were trigger time, stress phase, maximum amplitude, and median frequency. Here, phase denotes the normalized stress phase, Amp (dB) denotes the maximum amplitude of AE events, and Freq (kHz) denotes the median frequency. The parameter ε defines the neighborhood radius (distance threshold) for cluster formation, and MinPts specifies the minimum number of data points required within the ε-neighborhood. By configuring these two parameters, DBSCAN can capture variations in local data density and achieve robust clustering while effectively eliminating isolated noise components. The value of ε was selected from the elbow point of the k-distance plot, whereas MinPts was selected by comparing the silhouette score, number of clusters, and noise rate for candidate values ranging from 25 to 125. As an illustrative example, Fig. 7 presents the k-distance plots for the hydrogen-charged specimen tested at $\Delta K = 30\ MPa\sqrt{m}$. The elbow region was located at approximately 0.05; therefore, ε was set to 0.05. Thus, the DBSCAN parameters were not selected solely by visual inspection of the resulting clusters. For each dataset, ε was determined from the k-distance behavior, while candidate MinPts values were systematically evaluated using the silhouette score, number of clusters, and noise rate. The same parameter-selection procedure was applied to all test conditions. Because DBSCAN was applied independently to each test condition, the absolute distances in the normalized feature space and the resulting cluster labels were not assumed to be quantitatively equivalent between datasets. The clustering was used to identify persistent AE-event structures within each condition. The corresponding evaluation of candidate MinPts values is summarized in Table 3. The parameters for the remaining test conditions were selected using the same procedure and are listed in Table 4. For the uncharged specimen tested at $\Delta K = 30\ MPa\sqrt{m}$, the initial DBSCAN analysis showed lower silhouette scores and greater cluster fragmentation than the other conditions. Therefore, following the initial DBSCAN under the conditions listed in Table 4, a second round of DBSCAN was applied exclusively to a subset of the resulting clusters under the conditions specified in Table 5.

This secondary analysis was used only for the uncharged specimen at $\Delta K = 30\ MPa\sqrt{m}$ because the initial parameter screening produced comparatively low silhouette scores (0.065–0.26) and a large number of clusters (13–22), indicating insufficient separation of the AE-event groups. In contrast, the other conditions showed more distinct clustering under the initial analysis and therefore did not require further subdivision. The secondary DBSCAN was applied only to the unresolved subsets identified in the initial clustering, using the feature ranges and parameters listed in Table 5. For the uncharged specimen at $\Delta K = 30\ MPa\sqrt{m}$, the initial parameter screening yielded comparatively low silhouette scores and extensive cluster fragmentation. Therefore, the initial DBSCAN result was further subdivided only within unresolved subsets. The secondary analysis was not applied to the other conditions because their initial clustering provided sufficiently separated continuous AE-event groups.

Fig. 8 shows the AE occurrence behavior under each testing condition. The horizontal and vertical axes represent the testing time and the stress phase (phase), respectively; each plot indicates an individual AE event, with its color indicating the maximum amplitude. As shown in Fig. 6 showing definition of phase in one fatigue cycle, the phase is normalized, where the minimum and maximum load points are defined as 0 and 1, respectively. Since few AE events were detected during the unloading stage ($0.5 \leqq \text{phase} < 1.0$), the vertical axis ranges from 0 to 0.5. To display the full amplitude range across the three ΔK conditions, the color-bar scale was set to 50–80 dB for all plots; AE events with amplitudes below 65 dB or above 80 dB were plotted using the colors corresponding to 65 dB and 80 dB, respectively.

Clusters extracted by DBSCAN are shown in Fig. 9. Similar to Fig. 8, the horizontal and vertical axes represent the testing time and phase, respectively; each plot corresponds to an individual AE event, with its color indicating the assigned cluster. To enhance visual clarity, only the clusters of interest (i.e., those exhibiting stable, continuous curved distributions over a relatively long period) are color-coded, while the other events are colored gray. Colors are assigned to the clusters in ascending order of their average phase values; for instance, the cluster with the lowest phase under each testing condition is colored dark-blue. As demonstrated in Fig. 9, multiple curved AE event groups were successfully extracted under all testing conditions.

Table 6 compares the average phase of the dark-blue cluster (i.e., the cluster with the lowest phase) under each testing condition shown in Fig. 9. At all three ΔK levels, the lowest-phase AE cluster appeared at a lower average phase in the hydrogen-charged specimens than in the corresponding uncharged specimens. The lowest-phase cluster is interpreted here as an indicator of possible crack-opening-related activity because crack opening is expected to precede subsequent crack propagation during loading. However, the physical source of this cluster was not independently identified, and the cluster phase does not constitute a direct measurement of the crack-opening load,K_{op}.

Fatigue crack closure can arise from plasticity-induced, oxide-induced, and roughness-induced mechanisms. The respective contributions of these mechanisms could not be separated in the present experiments. Previous studies have reported hydrogen-induced changes in crack-tip deformation and crack-opening behavior in AISI 304 stainless steel; therefore, the earlier AE initiation observed after hydrogen charging is considered to be consistent with changes in crack-opening-related behavior. However, K_{op} and ΔK were not directly measured, and changes in these quantities cannot be established quantitatively from the present AE results. The primary mechanisms governing fatigue crack closure include plasticity-induced crack closure (PICC) [29], oxide-induced crack closure (OICC) [31], and roughness-induced crack closure (RICC) [32]. Particularly regarding PICC, Murakami et al. [17] reported that in AISI 304 austenitic stainless steel specimens charged with high-pressure hydrogen gas, slip deformation is localized near the crack tip, making the crack tip sharper than in the absence of hydrogen. Changes in crack-closure-related behavior, including PICC, may contribute to the earlier AE initiation observed after hydrogen charging. However, the respective contributions of plasticity-induced, oxide-induced, and roughness-induced crack closure could not be separated in the present experiments. Previous studies have shown that hydrogen can alter localized plastic deformation and crack-closure behavior in AISI 304 stainless steel. Such changes could reduce the crack-opening level and thereby modify the effective stress intensity factor range. In the present experiments, however, the crack-opening load, Kop, was not measured directly. Therefore, the earlier AE initiation observed in the hydrogen-charged specimens is interpreted only as being consistent with a change in crack-opening-related behavior, rather than as direct evidence of reduced K_{op} or increased ΔK_{eff}. In fact, the fractographic observation in Fig. 5 reveals quasi-cleavage fracture surfaces in the hydrogen-charged specimen. The quasi-cleavage morphology observed in the hydrogen-charged specimens is consistent with hydrogen-induced changes in the crack-tip deformation and fracture behavior. However, the fractographic observations are qualitative and do not directly

Table 3
Evaluation of candidate MinPts values for the hydrogen-charged and uncharged specimens at $\Delta K = 30\ MPa\sqrt{m}$ ($\varepsilon = 0.05$).

Charging condition	MinPts	Silhouette score	Number of clusters	Noise rate (%)
H-charged	25	0.21	11	3.9
	50	0.47	6	9.3
	75	0.21	8	12.0
	100	0.25	8	17.0
	125	0.52	5	26.0
Uncharged	25	0.11	13	0.76
	50	0.065	14	1.6
	75	0.20	20	2.4
	100	0.24	20	3.8
	125	0.26	22	5.5

Table 4
Parameters of each testing conditions for DBSCAN.

Test conditions		Parameters					
ΔK (MPa$\sqrt{m}$)	Charging	Time (s)	Phase	Amp. (dB)	Freq. (kHz)	ε	MinPts
30	Uncharged	0–25000	0.10–0.27	65–90	100–400	0.05	100
30	H-charged	0–4000	0.10–0.30	65–90	100–400	0.05	50
20	Uncharged	0–60000	0.17–0.30	60–90	100–400	0.05	50
20	H-charged	0–9000	0.15–0.30	60–90	100–400	0.05	50
15	Uncharged	0–160000	0.20–0.40	50–70	100–400	0.05	50
15	H-charged	0–16000	0.15–0.40	50–70	100–400	0.05	50

Table 5
Secondary DBSCAN conditions for the uncharged specimen at $\Delta K = 30$ MPa$\sqrt{m}$.

	Time (s)	Phase	Amp. (dB)	Freq. (kHz)	ε	MinPts
1	14000-23500	0.14-0.20	65-81	100-400	0.02	50
2	2100-14900	0.14-0.23	65-85	100-400	0.09	100

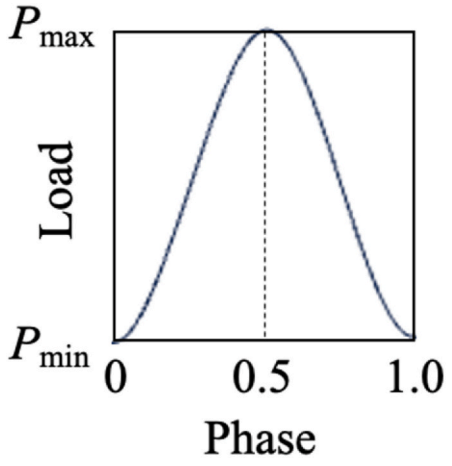


Fig. 6. Definition of stress phase normalization.

quantify the extent of crack-tip plastic deformation or the contribution of plasticity-induced crack closure. Furthermore, Table 6 shows that the average phase of the lowest-phase cluster varied from 0.18 to 0.29 across the three ΔK conditions for the uncharged specimens, whereas values of 0.15–0.18 were obtained for the hydrogen-charged specimens. Thus, a smaller apparent variation with ΔK was observed after hydrogen charging within the tested range. Because only three ΔK levels were examined and uncertainty in the cluster-average phase was not statistically quantified, this observation is interpreted as a trend rather than as evidence of a statistically significant suppression of ΔK dependence.

Fig. 10 shows the time evolution of the peak frequency for the AE clusters under each testing condition. The color coding of each cluster corresponds to that in Fig. 9. For both the uncharged and hydrogen-charged specimens, the peak frequency of every cluster remained virtually constant throughout the testing duration. For both uncharged and hydrogen-charged specimens, the peak frequency of each selected cluster remained relatively stable throughout the corresponding test. This spectral consistency supports the interpretation that the events within a cluster exhibit similar AE characteristics. However, peak frequency alone cannot uniquely identify an AE source mechanism because the measured spectrum is also influenced by wave propagation, sensor response, specimen geometry, attenuation, coupling, and acquisition conditions. Therefore, the present results do not establish that all events within a cluster originate from an identical physical mechanism. Based on the above-mentioned hypothesis—that AE events generated during the loading process originate from crack propagation or crack opening—each curve can be interpreted as corresponding to crack propagation or crack-face friction within a specific local region. However, further investigation is required to conclusively identify the detailed underlying mechanisms.

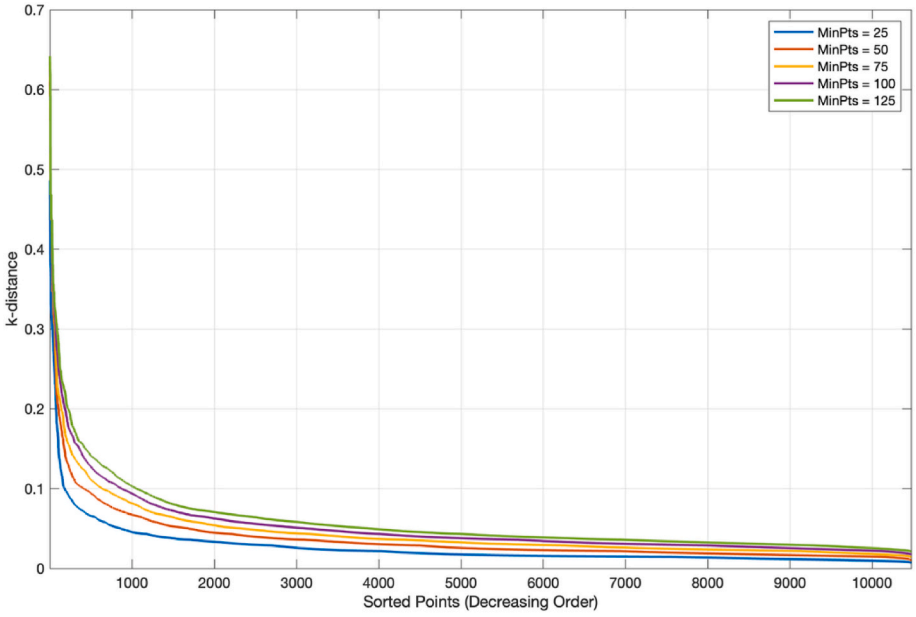


Fig. 7. k-distance plots for candidate MinPts values (25–125) for the hydrogen-charged specimen tested at ΔK = 30 MPa$\sqrt{m}$, used to select the DBSCAN neighborhood radius, ε.

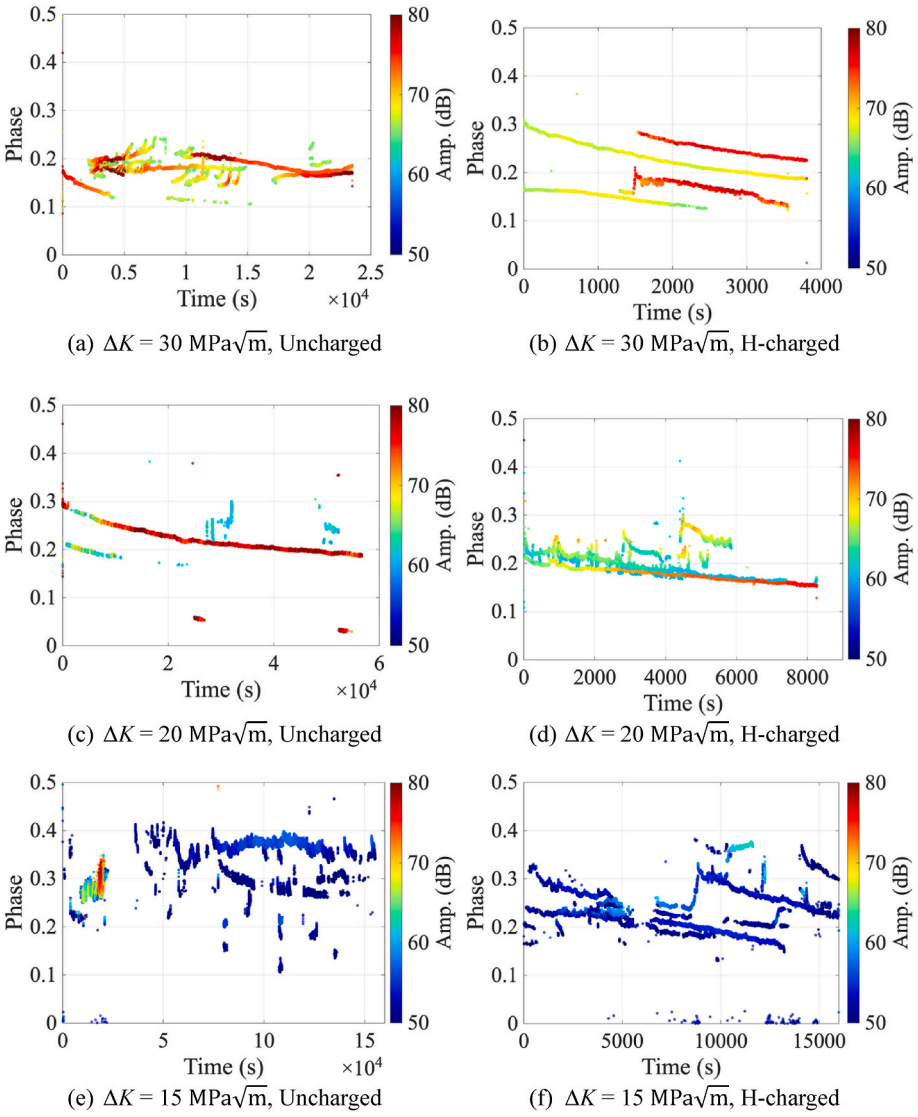


Fig. 8. Stress phase transition of AE events.

Furthermore, Fig. 10 indicates that in the uncharged specimen, the peak frequency tended to increase with decreasing ΔK, shifting from 200 to 230 kHz at $\Delta K = 30$ MPa$\sqrt{\text{m}}$ to approximately 250 kHz at $\Delta K = 15$ MPa$\sqrt{\text{m}}$. In contrast, the hydrogen-charged specimen exhibited a peak frequency of around 190 kHz across all ΔK levels. This implies that the presence of hydrogen suppressed the influence of ΔK on the crack propagation behavior. Previous studies have reported hydrogen-induced changes in crack-tip plastic deformation and strain-induced martensitic transformation in AISI 304 stainless steel [8–10] and retards strain-induced martensitic transformation by increasing austenite stability [2,11,12]. The amount of strain-induced martensitic transformation is known to depend on ΔK [33]. However, neither the local plastic deformation nor the martensite fraction was directly quantified in the specimens used for the present AE measurements. Therefore, the observed peak-frequency differences cannot be uniquely attributed to either mechanism. They are interpreted here only as indicating differences in the AE characteristics associated with crack-tip deformation and crack-propagation behavior. The suppression of these variations by hydrogen is considered the primary factor that reduced the differences in frequency characteristics among the different ΔK levels. It should be noted, however, as discussed later, that the martensitic transformation itself was likely undetectable by the AE method in our study. The observed peak-frequency differences may reflect changes in crack-tip deformation and crack-propagation behavior; the underlying source mechanisms could not be uniquely identified in the present study.

3.4. Detection of martensitic transformation by AE

Martensitic transformation is a diffusionless process that does not involve atomic diffusion; instead, the crystal structure undergoes collective shear deformation to relieve lattice strain. Consequently, although individual transformation events occur at high speeds and exhibit a burst-type nature at the microscopic scale, macroscopic AE measurements are expected to exhibit continuous behavior due to the superposition of countless transformation events. Indeed, van Bohemen et al. [34] measured AE during the continuous cooling of carbon steel and reported that the AE signals exhibited continuous behavior resulting from the accumulation of numerous nucleation events.

As a representative example in this study, Fig. 11 shows the AE RMS voltage at $\Delta K = 30$ MPa$\sqrt{\text{m}}$. The blue and green lines represent the load signal and the AE RMS voltage, respectively. The horizontal axis indicates time, whereas the left and right vertical axes represent the load signal voltage and the RMS voltage, respectively. No significant continuous AE signals attributable to the transformation were observed in either the uncharged or hydrogen-charged specimens.

Takeda et al. [20] previously conducted constant-ΔK fatigue tests

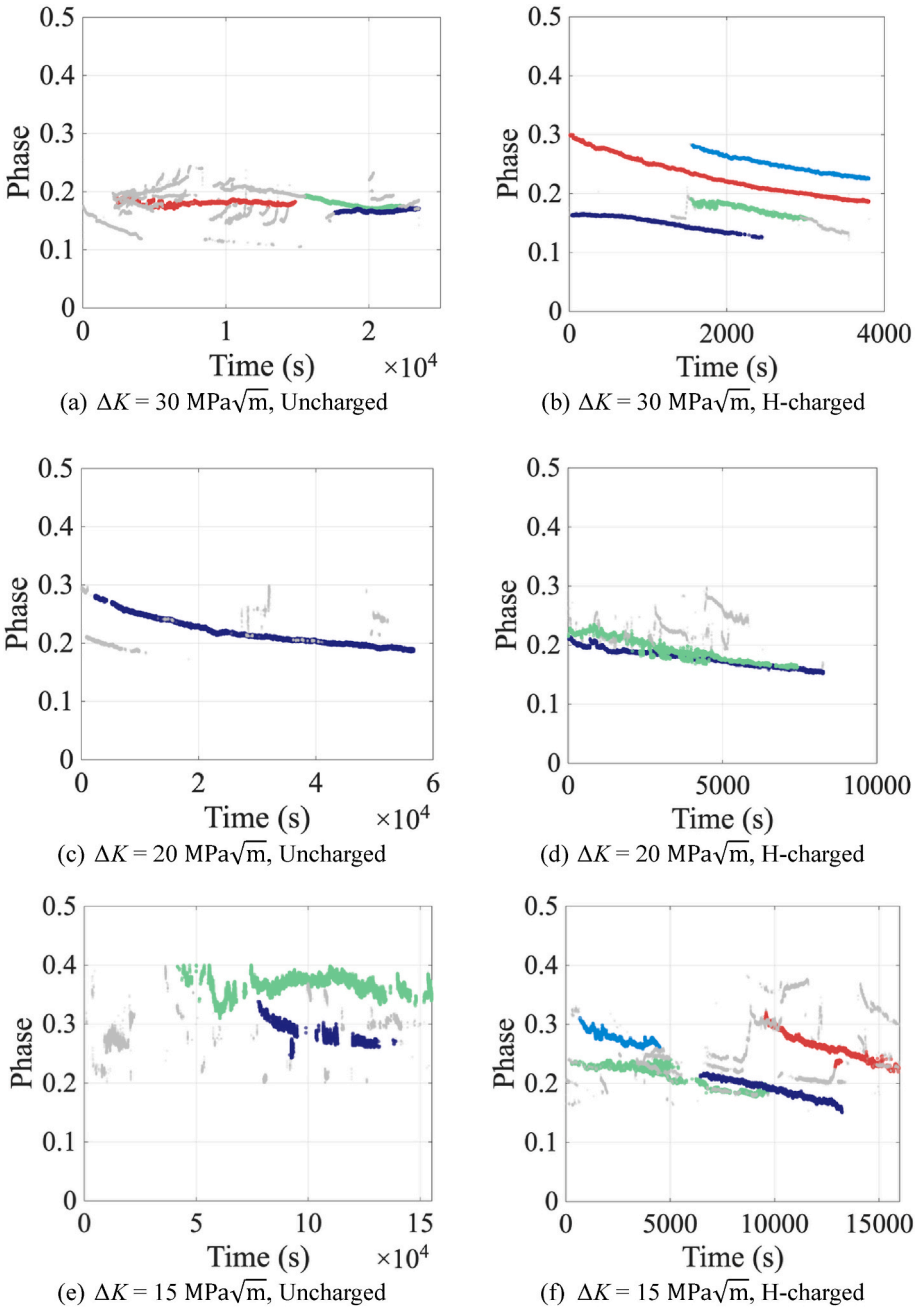


Fig. 9. DBSCAN clustering results of AE events, with clusters color-coded in ascending order of their average phase values. (For interpretation of the references to color in this figure legend, the reader is referred to the Web version of this article.)

Table 6
Comparison of the average phase of the lowest-phase AE clusters (dark-blue clusters in Fig. 9) under each testing condition.

	Uncharged	H-charged
$\Delta K = 30\ \mathrm{MPa}\sqrt{\mathrm{m}}$	0.18	0.15
$\Delta K = 20\ \mathrm{MPa}\sqrt{\mathrm{m}}$	0.22	0.18
$\Delta K = 15\ \mathrm{MPa}\sqrt{\mathrm{m}}$	0.29	0.18

using the same heat of AISI 304 austenitic stainless steel, specimen geometry, and testing conditions as those used in the present study. Their post-test EBSD observations confirmed the formation of martensite around the fatigue crack in the uncharged specimens, whereas little martensite was observed in the hydrogen-charged specimens, indicating that hydrogen charging suppressed martensitic transformation. Thus, although martensitic transformation is expected to have occurred around the fatigue crack in the uncharged specimens in the present study, no corresponding continuous AE signals were clearly detected. Thus, although martensitic transformation was expected to occur around the fatigue crack based on the previous EBSD study using the same material heat and testing conditions, no AE response uniquely attributable to martensitic transformation was identified in the present experiments. Accordingly, martensitic transformation could not be directly identified by AE under the present experimental conditions. However, the martensite fraction was not measured directly in the specimens used for the present AE experiments. Therefore, the results of Takeda et al. are used only as supporting evidence for the expected microstructural tendency under comparable conditions and not as a direct measurement of martensite content in the present specimens.

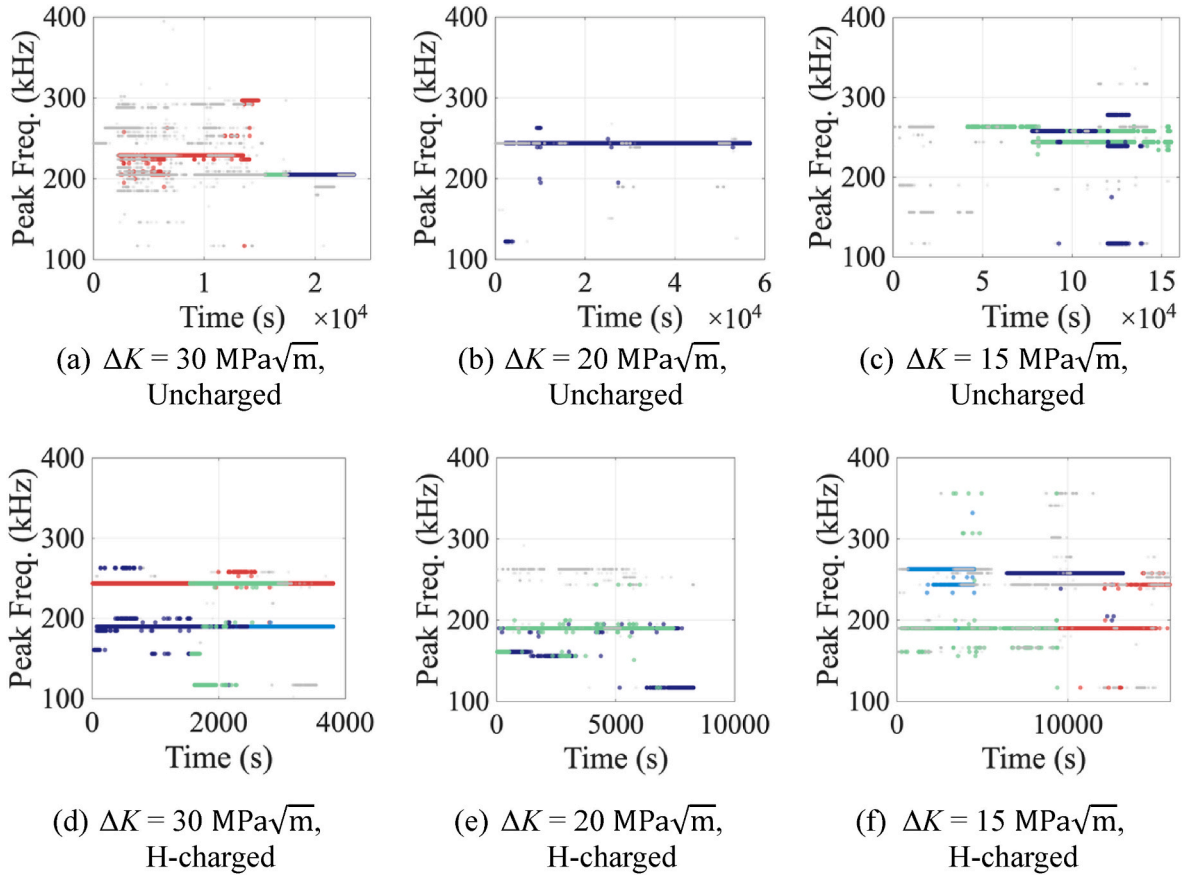


Fig. 10. Peak frequency transition of AE clusters (The color coding of each cluster corresponds to Fig. 9). (For interpretation of the references to color in this figure legend, the reader is referred to the Web version of this article.)

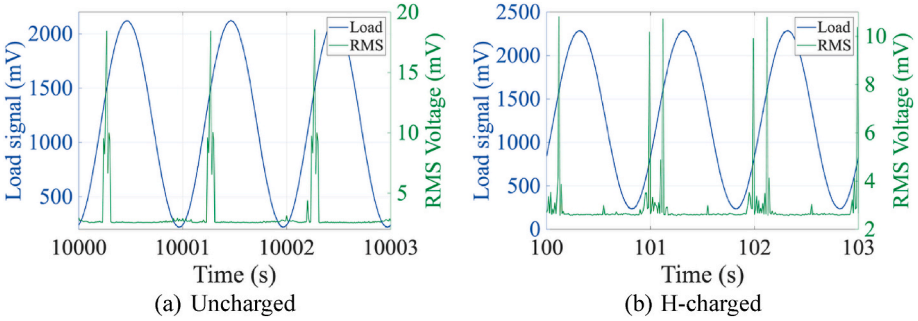


Fig. 11. Load signals and RMS voltage under $\Delta K = 30$ MPa$\sqrt{\text{m}}$.

4. Conclusion

This study evaluated the effects of hydrogen on fatigue crack propagation in AISI 304 austenitic stainless steel by multi-parameter analysis of AE. Real-time AE measurements were conducted during fatigue crack propagation tests on hydrogen-charged and uncharged specimens under constant ΔK conditions, and the detected AE events were classified using a DBSCAN algorithm. The primary findings are summarized as follows:

(1) Hydrogen-charged specimens exhibited AE initiation at a lower stress phase than the corresponding uncharged specimens. Across the three tested ΔK conditions, the hydrogen-charged specimens also showed a smaller apparent variation in the initiation phase. The lowest-phase AE cluster was interpreted as an indicator of possible crack-opening-related activity; however, Kop and ΔKeff were not directly measured. Therefore, the observed phase shift is considered to be consistent with hydrogen-induced changes in crack-opening and crack-tip deformation behavior rather than direct evidence of reduced plasticity-induced crack closure.

(2) The peak frequency of the selected AE clusters remained relatively stable during each fatigue test, supporting consistency in the characteristics of the clustered AE events. The uncharged specimens showed an apparent change in peak frequency among the three ΔK conditions, whereas smaller differences were observed for the hydrogen-charged specimens. These frequency differences may reflect changes in crack-tip deformation and crack-propagation behavior; however, the underlying AE source mechanisms could not be uniquely identified.

(3) No significant AE signals attributable to martensitic transformation, which is considered as one of the factors of HE in

metastable stainless steels, were detected in the AE RMS voltage measurements for both the uncharged and hydrogen-charged specimens.

CRediT authorship contribution statement

Ryutaro Matsumoto: Writing – review & editing, Writing – original draft, Visualization, Validation, Software, Methodology, Investigation, Data curation, Conceptualization. **Kaita Ito:** Writing – review & editing, Supervision, Software, Formal analysis. **Luthfan Adhy Lesmana:** Writing – review & editing, Supervision, Project administration. **Takashi Iijima:** Resources, Methodology. **Hirotoshi Enoki:** Supervision, Methodology. **Tetsuya Uchimoto:** Writing – review & editing, Supervision, Project administration, Funding acquisition.

Declaration of competing interest

The authors declare that they have no known competing financial interests or personal relationships that could have appeared to influence the work reported in this paper.

References

[1] Itaoka K, Kimura S, Hirose K. Methodology development to locate hydrogen stations for the initial deployment stage. E3S Web Conf 2019;83:01014. https://doi.org/10.1051/e3sconf/20198301014.

[2] Ogawa Y, Okazaki S, Takakuwa O, Matsunaga H. The roles of internal and external hydrogen in the deformation and fracture processes at the fatigue crack tip zone of metastable austenitic stainless steels. Scr Mater 2018;157:95–9. https://doi.org/10.1016/j.scriptamat.2018.08.003.

[3] Zhang L, Wen M, Imade M, Fukuyama S, Yokogawa K. Effect of nickel equivalent on hydrogen gas embrittlement of austenitic stainless steels based on type 316 at low temperatures. Acta Mater 2008;56:3414–21. https://doi.org/10.1016/j.actamat.2008.03.022.

[4] Merson ED, Myagkikh PN, Poluyanov VA, Merson DL, Vinogradov A. Quasi-cleavage hydrogen-assisted cracking path investigation by fractographic and side surface observations. Eng Fract Mech 2019;214:177–93. https://doi.org/10.1016/j.engfracmech.2019.04.042.

[5] Mine Y, Koga K, Kraft O, Takashima K. Mechanical characterisation of hydrogen-induced quasi-cleavage in a metastable austenitic steel using micro-tensile testing. Scr Mater 2016;113:176–9. https://doi.org/10.1016/j.scriptamat.2015.11.013.

[6] Koyama M, Akiyama E, Sawaguchi T, Ogawa K, Kireeva IV, Chumlyakov YI, Tsuzaki K. Hydrogen-assisted quasi-cleavage fracture in a single crystalline type 316 austenitic stainless steel. Corros Sci 2013;75:345–53. https://doi.org/10.1016/j.corsci.2013.06.018.

[7] Martin ML, Fenske JA, Liu GS, Sofronis P, Robertson IM. On the formation and nature of quasi-cleavage fracture surfaces in hydrogen embrittled steels. Acta Mater 2011;59:1601–6. https://doi.org/10.1016/j.actamat.2010.11.024.

[8] Martin ML, Dadfarnia M, Nagao A, Wang S, Sofronis P. Enumeration of the hydrogen-enhanced localized plasticity mechanism for hydrogen embrittlement in structural materials. Acta Mater 2019;165:734–50. https://doi.org/10.1016/j.actamat.2018.12.014.

[9] Nagumo M, Yoshida H, Shimomura Y, Kadokura T. Ductile crack growth resistance in hydrogen-charged steels. Mater Trans 2001;42:132–7. https://doi.org/10.2320/matertrans.42.132.

[10] Birnbaum HK, Sofronis P. Hydrogen-enhanced localized plasticity—a mechanism for hydrogen-related fracture. Mater Sci Eng, A 1994;176:191–202. https://doi.org/10.1016/0921-5093(94)90975-X.

[11] Mine Y, Horita Z, Murakami Y. Effect of hydrogen on martensite formation in austenitic stainless steels in high-pressure torsion. Acta Mater 2009;57:2993–3002. https://doi.org/10.1016/j.actamat.2009.03.006.

[12] Narita N, Altstetter CJ, Birnbaum HK. Hydrogen-related phase transformations in austenitic stainless steels. Metall Trans A 1982;13:1355–65. https://doi.org/10.1007/BF02642872.

[13] Oriani RA. A mechanistic theory of hydrogen embrittlement of steels. Ber Bunsen Ges Phys Chem 1972;76:848–57. https://doi.org/10.1002/bbpc.19720760864.

[14] Troiano AR. The role of hydrogen and other interstitials in the mechanical behavior of metals. Metallogr Microstruct Anal 2016;5:557–69. https://doi.org/10.1007/s13632-016-0319-4.

[15] Beachem CD. A new model for hydrogen-assisted cracking (hydrogen "embrittlement"). Metall Trans A 1972;3:441–55. https://doi.org/10.1007/BF02642048.

[16] Djukic MB, Bakic GM, Sijacki Zeravcic V, Sedmak A, Rajicic B. The synergistic action and interplay of hydrogen embrittlement mechanisms in steels and iron: localized plasticity and decohesion. Eng Fract Mech 2019;216:106528. https://doi.org/10.1016/j.engfracmech.2019.106528.

[17] Murakami Y, Kanezaki T, Mine Y, Matsuoka S. Hydrogen embrittlement mechanism in fatigue of austenitic stainless steels. Metall Mater Trans A 2008;39:1327–39. https://doi.org/10.1007/s11661-008-9506-5.

[18] Koyama M, Springer H, Merzlikin SV, Tsuzaki K, Akiyama E, Raabe D. Hydrogen embrittlement associated with strain localization in a precipitation-hardened Fe–Mn–Al–C light weight austenitic steel. Int J Hydrogen Energy 2014;39:4634–46. https://doi.org/10.1016/j.ijhydene.2013.12.171.

[19] Choo WY, Lee JY. Thermal analysis of trapped hydrogen in pure iron. Metall Trans A 1982;13:135–40. https://doi.org/10.1007/BF02642424.

[20] Takeda S, Ohara Y, Uchimoto T, Enoki H, Iijima T, Tokuda E, Yamada T, Nagatomo Y. Characterization of fatigue crack of hydrogen-charged austenitic stainless steel by electromagnetic and ultrasonic techniques. Int J Hydrogen Energy 2022;47:32223–34. https://doi.org/10.1016/j.ijhydene.2022.07.105.

[21] Dunegan HL, Tetelman AS. Non-destructive characterization of hydrogen-embrittlement cracking by acoustic emission techniques. Eng Fract Mech 1971;2:387–402. https://doi.org/10.1016/0013-7944(71)90021-X.

[22] Shiraiwa T, Kawate M, Briffod F, Kasuya T, Enoki M. Evaluation of hydrogen-induced cracking in high-strength steel welded joints by acoustic emission technique. Mater Des 2020;190:108573. https://doi.org/10.1016/j.matdes.2020.108573.

[23] Jiang X, Shen X, Gao R, Rao J, Xing B, Hua Z. Investigation of hydrogen-induced crack acoustic emission response law of 304 austenitic stainless steel at different temperatures. Int J Hydrogen Energy 2026;199:152857. https://doi.org/10.1016/j.ijhydene.2025.152857.

[24] American Society for Testing and Materials. Committee E08 on Fatigue and Fracture, Standard test method for measurement of fatigue crack growth rates. American Society of Testing Materials; 2008.

[25] Ito K, Enoki M. Acquisition and analysis of continuous acoustic emission waveform for classification of damage sources in ceramic fiber mat. Mater Trans 2007;48:1221–6. https://doi.org/10.2320/matertrans.I-MRA2007850.

[26] Ito K, Kuriki H, Watanabe M, Kuroda S, Enoki M. Detection of AE events due to cracks in TBC during spraying process. Mater Trans 2012;53:671–5. https://doi.org/10.2320/matertrans.MBW201118.

[27] Ito K, Kuriki H, Araki H, Kuroda S, Enoki M. Detection of segmentation cracks in top coat of thermal barrier coatings during plasma spraying by non-contact acoustic emission method. Sci Technol Adv Mater 2014;15:035007. https://doi.org/10.1088/1468-6996/15/3/035007.

[28] Ester M, Kriegel H-P, Sander J, Xu X. A density-based algorithm for discovering clusters in large spatial databases with noise. In: Proceedings of the Second International Conference on Knowledge Discovery and Data Mining (KDD-96). AAAI Press; 1996. p. 226–31.

[29] Elber W. The significance of fatigue crack closure, 486. ASTM STP; 1971. p. 230–42.

[30] Nonaka K, Sekine K, Ieki T. In-Situ observation and AE monitoring of fatigue crack propagation in SUS304 steel. Anzen Kogaku 1989;28:18–25. https://doi.org/10.18943/safety.28.1_18.

[31] Suresh S, Zamiski GF, Ritchie DRO. Oxide-induced crack closure: an explanation for near-threshold corrosion fatigue crack growth behavior. Metall Trans A 1981;12:1435–43. https://doi.org/10.1007/BF02643688.

[32] Walker N, Beevers CJ. A fatigue crack closure mechanism in titanium. Fatig Fract Eng Mater Struct 1979;1:135–48. https://doi.org/10.1111/j.1460-2695.1979.tb00372.x.

[33] Mei Z, Morris JW. Influence of deformation-induced martensite on fatigue crack propagation in 304-type steels. Metall Trans A 1990;21:3137–52. https://doi.org/10.1007/BF02647310.

[34] van Bohemen SMC, Sietsma J, Hermans MJM, Richardson IM. Kinetics of the martensitic transformation in low-alloy steel studied by means of acoustic emission. Acta Mater 2003;51:4183–96. https://doi.org/10.1016/S1359-6454(03)00236-2.